INTERNATIONAL JOURNAL FOR NUMERICAL METHODS IN FLUIDS
Int. J. Numer. Meth. Fluids 2003; **43**:407–430 (DOI: 10.1002/fld.580)

Computation of turbulent free-surface flows around modern ships

Tingqiu Li*,†

Ship Laboratory, Helsinki University of Technology, Finland

SUMMARY

This paper presents the calculated results for three classes of typical modern ships in modelling of ship-generated waves. Simulations of turbulent free-surface flows around ships are performed in a numerical water tank, based on the FINFLO-RANS SHIP solver developed at Helsinki University of Technology. The Reynolds-averaged Navier–Stokes (RANS) equations with the artificial compressibility and the non-linear free-surface boundary conditions are discretized by means of a cell-centred finite-volume scheme. The convergence performance is improved with the multigrid method. A free surface is tracked using a moving mesh technology, in which the non-linear free-surface boundary conditions are given on the actual location of the free surface. Test cases recommended are a container ship, a US Navy combatant and a tanker. The calculated results are compared with the experimental data available in the literature in terms of the wave profiles, wave pattern, and turbulent flow fields for two turbulence models, Chien's low Reynolds number k–ε model and Baldwin–Lomax's model. Furthermore, the convergence performance, the grid refinement study and the effect of turbulence models on the waves have been investigated. Additionally, comparison of two types of the dynamic free-surface boundary conditions is made. Copyright © 2003 John Wiley& Sons, Ltd.

KEY WORDS: turbulent non-linear free-surface flows; modern ships with a transom; a moving mesh technology; FINFLO-RANS SHIP solver

1. INTRODUCTION

Modelling of turbulent free-surface flows around a practical structure is of significance in ship design and ocean engineering using the computational fluids dynamics (CFD) techniques. An elucidation of such detailed mechanisms is always desirable for research in hydrodynamics. It is one of the main interests of industry. Recent advance in CFD numerical schemes provides the possibility for this purpose. Most codes available currently are through resolution of the mathematical model of the Reynolds–averaged Navier–Stokes (RANS) equations with closure of a turbulence model. A flow characteristic may be described by two major independent parameters: the Reynolds number (R_n) and the Froude number (F_n).

*Correspondence to: Tingqiu Li, Department of Civil Engineering, University of Ghent, Technologiepark 904, B-9052, Zwijnaarde, Belgium.
† E-mail: tingqiu.li@rug.ac.be

Received January 2002
Revised 19 February 2003

A free surface associated with the water waves exists owing to the F_n effect. Typical example is fluid–structure interaction problems like ship wavemaking. Dependent on whether the grid adapts to the shape and position of the free surface, two major approaches widely applied to the free-surface computations are the so-called interface-tracking method, e.g. a moving mesh [1–5], and the interface-capturing method, e.g. the volume-of-fluid (VOF) method and the level set schemes [6–8]. The former is to introduce a mesh that moves over an underlying fixed Eulerian grid for explicitly tracking a free surface referred as an air–water interface. This mesh only covers the domain involving the water, where the free surface forms the upper boundary of the computational domain and is determined as part of the solution. The boundary conditions at the interface are prescribed on the actual location of the surface. No smearing of the interface is involved during tracking. As a result, a high order of accuracy may be preserved. The precise location and geometry of the interface can be given. This approach can be applied for moving boundary problems due to the fact that desirable information of the interface is available. In this procedure, the free-surface elevation may be described by the kinematic free-surface boundary condition (KFSBC); the implementation of the dynamic free-surface boundary conditions on the exact location of the interface transmits information of the interface into the grid. The new volumetric grid has to be reconstructed in order to follow the motion of the interface. Nevertheless, this restricts an application in a large deformation like the breaking waves unless ad hoc treatments (for example, a wave slope) are employed. Instead of the use of the deformed mesh, the capturing method is able to deal with the breaking waves in a fixed mesh, which implicitly prescribes the boundary conditions at the interface in most cases. But, it requires specific advection schemes so that the sharpness of the interface front is preserved. More accurate prediction is dependent on the grid resolution. Based on the VOF method, an arbitrary Lagrangian–Eulerian (ALE) approach tends to be more flexible [9]. In this way, the Lagrangian scheme is used to explicitly track the interfacial discontinuity, while the solution for the bulk flow is obtained on a fixed Eulerian grid. The following is mainly to emphasize numerical aspects within the framework of the moving-mesh technique, some of which are also suitable for the capturing method.

For a turbulent flow, large number of grid points have to be distributed inside the boundary layer, while describing the complex features of the geometry. On the other hand, a relatively fine mesh is constructed in the outer flow so that the more detailed structure of the wave systems can be captured. To merge these features, one approach is to utilize more grids: one for the free surface and another for the bulk flow. They are connected to each other with an interpolation interface [10, 11]. An alternative is to construct one grid but allow multiblock boundaries, which tends to be one of the most common approaches [2–6].

Generally, two categories, an uncoupled algorithm and a fully coupled algorithm, are classified for the solution of the RANS solvers with interfaces. In the latter case, a global mass conservation is maintained in that the interface and the bulk RANS evolution are updated simultaneously by sweeping over the entire domain. Consequently, a full coupling is achieved [12, 13]. One advantage is that the convergence rate is improved significantly [14]. In the former case, the bulk RANS flow is solved iteratively under all the known boundary conditions together with the distribution of the wave elevation. Thus, the full coupling over the subdomains between the RANS flow and the free surface is not enforced at one currently iterative cycle. This is relatively straightforward in its implementation within a flexible framework for modifying and adapting a method due to the complexities of the coupled approach [15]. One of the dynamic free-surface boundary conditions, for example, is applied as the

Dirichlet boundary condition for the pressure. A high quality of grid generation relied on the updated wave height can be ensured.

Due to the combined effects of R_n and F_n, a problem related to the numerical singularity at the contact line (that is, at the intersection of the free surface with a hull surface) should be addressed. It states that the integration of the KFSBC will give rise to a singular solution at this line due to the no-slip constraints on a hull. It comes from the kinematic incompatibility by the fact that the physical phenomenon of $\partial h/\partial t = 0$ (see Equation (6), where h is the wave elevation and t is the time) on the hull is not observed during a whole experimental visualization. To remove the kinematic paradox in mathematics, one approach popular is to extrapolate the wave elevation in the first cell to the hull surface based on the assumption that the flow at this cell becomes tangential to the hull surface. Thus, a numerical displacement at the contact point is asymptotically satisfied. An alternative is to express the flux on the free surface by the enforcement of the mass conservation [16]. Without extrapolation, therefore, the wave height on the hull surface can be evaluated by averaging the velocity on the face of the control volume surrounding a cell of the wave height.

Since meshes within the boundary layer are sufficiently refined for accurate calculation of skin friction resistance, such feedback can induce undesirable numerical instability in the free-surface computations due to high wave numbers. This causes oscillations of the waves at the grid scale. Moreover, lack of numerical dissipation for higher-order schemes results in an unstable numerical system [5]. Therefore, the two approaches above mentioned appear to be insufficient to overcome such problems associated with oscillations. Additionally, numerical simulations have to identify a characteristic of modern ship forms, such as the breaking waves occurred at a bulbous bow or due to a sonar dome, and more complex flow patterns off a transom stern. For the transom flow, this is a challenging problem, especially for a partially wetted transom [17].

Numerous attempts have been made to deal with these situations, some of which are served the function of numerical dissipation as follows: to add a high-order artificial dissipation term into the KFSBC [11, 18]; to locally introduce the lower order dissipation [1]; and to filter the free surface [4]. These can enhance numerical stability through avoiding the overturning waves and/or eliminating spurious oscillations. Interestingly, one approach [5, 19] is to give a finite thickness α (where α is constant for all time) for approximation of the width of the interface [19] or the contact line [5]. The former can be applied to resolve a discontinuous jump of the density ρ when passing through the interface, especially for large density ratios; the latter is used for interpolated region of the wave elevation in order to cope with a grid that is highly clustered in the near-wall spacing. For transom stern ships concerned, the so-called dry-transom model could be implemented [20–22]. The relevant work can be found in References [23–25].

In this paper, the FINFLO-RANS solver will be applied to numerical simulation of three-dimensional turbulent free-surface flows around modern transom stern ships. This is an uncoupled approach. A cell-centred finite-volume multigrid scheme is implemented for the solution of the three-dimensional RANS equations with the artificial compressibility. A free surface is tracked using a moving mesh. In addition, an approach of solution of the free surface is explored and incorporated into this solver, in which the non-linear free-surface boundary conditions are discretized on the basis of a cell-centred finite-volume method with the ENO type and a model for approximating the near-wall free surface is introduced. This helps to maintain stabilization of the free surface and provides one possibility for improvement of our

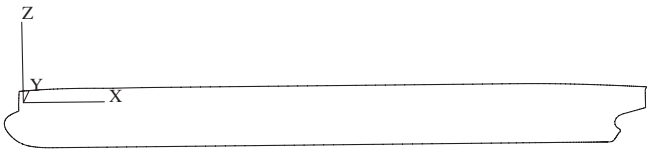

Figure 1. A reference co-ordinate system around a ship.

technique competence [26]. Moreover, two classes of the dynamic free-surface boundary conditions are compared. The steady-state computations are performed with two selected transom types: a dry or a partially wetted transom. Finally, the convergence performance, the grid dependence and the effect of turbulence models on the waves will be investigated by means of two turbulence models, Chien's low Reynolds number k–ε model and Baldwin–Lomax's model. Three examples are presented in this paper. The first one involves the KRISO container ship (KCS) model; the second one a US Navy combatant, DTMB 5415 model; and the last one a tanker model from the shipyard, Kvaerner Masa-Yards, Finland. Methodology including the mathematical models, the initial and the boundary conditions and the numerical solution is briefly described in Section 2; and then the computational conditions and the results in the steady-state as well as discussions are given for these three cases in Sections 3 and 4; finally some concluding remarks are made in Section 5.

2. METHODOLOGY

2.1. Mathematical models

On the Cartesian co-ordinate system of a right hand (x, y, z), the three-dimensional RANS equations can be written in the compact form, where the origin O is fixed at the intersection of the bow with the still free surface, x is positive in the aft direction, y is positive towards the port and the z-direction is positive upwards (see Figure 1). Namely

$$\frac{\partial U}{\partial t} + \frac{\partial (F - F_v)}{\partial x} + \frac{\partial (G - G_v)}{\partial y} + \frac{\partial (H - H_v)}{\partial z} = Q \tag{1}$$

where the variable $U = (\rho, \rho u, \rho v, \rho w)^{\mathrm{T}}$. The inviscid fluxes (F, G, H), the viscous fluxes (F_v, G_v, H_v) and the source term (Q) are expressed as a usual tradition [27], respectively. ρ is the density of the fluid, and the mean-velocity components in the x-, y- and z-directions are denoted by (u, v, w). To evaluate the turbulent viscous coefficient μ_{t}, Chien's low Reynolds number k–ε turbulence model [28] is implemented. It reads as

$$\begin{aligned}
\frac{\partial \rho k}{\partial t} + \frac{\partial \rho u k}{\partial x} + \frac{\partial \rho v k}{\partial y} + \frac{\partial \rho w k}{\partial z} &= \left(\mu + \frac{\mu_{\mathrm{t}}}{\sigma_k}\right)\left\{\frac{\partial^2 k}{\partial x^2} + \frac{\partial^2 k}{\partial y^2} + \frac{\partial^2 k}{\partial z^2}\right\} + G_1 \\
\frac{\partial \rho \varepsilon}{\partial t} + \frac{\partial \rho u \varepsilon}{\partial x} + \frac{\partial \rho v \varepsilon}{\partial y} + \frac{\partial \rho w \varepsilon}{\partial z} &= \left(\mu + \frac{\mu_{\mathrm{t}}}{\sigma_\varepsilon}\right)\left\{\frac{\partial^2 \varepsilon}{\partial x^2} + \frac{\partial^2 \varepsilon}{\partial y^2} + \frac{\partial^2 \varepsilon}{\partial z^2}\right\} + G_2
\end{aligned} \tag{2}$$

Table I. Empirical coefficients in the k–ε model.

c_1	c_2	σ_k	σ_ε	c_μ
1.44	$1.92(1-0.22e^{-Re_t^2/36})$	1.0	1.3	$0.09(1-e^{-0.0115y^+})$

with G_1 and G_2

$$G_1 = P - \rho\varepsilon - 2\mu\frac{k}{d^2}$$
$$G_2 = c_1\frac{\varepsilon}{k}P - c_2\frac{\rho\varepsilon^2}{k} - 2\mu\frac{\varepsilon}{d^2}e^{-y^+/2}$$

where k and ε are the turbulent kinetic energy and its dissipation of turbulence, respectively. P is the production of turbulent kinetic energy defined as

$$P = \left\{\mu_t\left(\frac{\partial u_i}{\partial x_j} + \frac{\partial u_j}{\partial x_i} - \frac{2}{3}\delta_{ij}\frac{\partial u_k}{\partial x_k}\right) - \frac{2}{3}\rho k\delta_{ij}\right\}\frac{\partial u_i}{\partial x_j} \tag{3}$$

according to tensor notation ($i, j = 1, 2, 3$). δ_{ij} is the Kronecker's symbol and $\mu = \rho\nu$ (ν is the kinematic viscosity of 1.01×10^{-6}). Additionally, it is enforced as $P = \min(P, 20\rho\varepsilon)$ so that an unphysical phenomena is avoided [29]. Owing to a strong interaction of the flow with the turbulent quantities, the pseudo-linear form is introduced [30]. With the normal distance from the wall d, y^+ is defined as

$$y^+ = d\left\{\frac{\rho\,|\nabla\times\mathbf{V}|}{\mu}\right\}_w^{1/2} \tag{4}$$

where the subscript (w) denotes over the wall surface, and $\mathbf{V} = u\mathbf{i} + v\mathbf{j} + w\mathbf{k}$. Finally, μ_t is evaluated by

$$\mu_t = c_\mu\frac{\rho k^2}{\varepsilon} \tag{5}$$

With this model, the solution is allowed to extend to a wall instead of the use of a wall function [31]. It is performed with the damping function that describes reduction of turbulence according to a turbulent Reynolds number, $Re_t = \rho k^2/\mu\varepsilon$. Empirical coefficients employed in this model are given in Table I.

2.2. Initial and boundary conditions

The computational domain consists of six planes that apply the boundary conditions: the inlet, the outlet, the hull surface, the centreline boundary, the external boundary and the free surface. Since it is an initial–boundary value problem, the initial and boundary conditions are specified as follows.

For the initial conditions, a free-stream pressure, a uniform flow and a zero wave height are given. A constant distribution of the turbulent quantities is specified.

For the boundary conditions, no-slip conditions and $k = \mu_t = 0$ are imposed on the wetted part of the hull surface, while the pressure on this surface is extrapolated by the Neumann condition. At the inlet, a uniform flow is specified and the constant distribution of the turbulent quantities is given. At the outlet, all variables are extrapolated with a zero-gradient approach. On the centreline boundary and the external boundary, the mirror conditions for all variables are employed. k and ε on the free surface are set by the mirror condition. In this paper, the focus involves mainly the solution of the non-linear free-surface boundary conditions.

2.3. *Free-surface boundary conditions*

The boundary conditions on the free surface are given with one kinematic and three dynamic conditions in the following way.

2.3.1. The kinematic free-surface boundary condition (KFSBC). Within the Cartesian co-ordinate system, the KFSBC is formulated with the following two-dimensional (2D) hyperbolic wave equation:

$$\frac{\partial h}{\partial t} + u\frac{\partial h}{\partial x} + v\frac{\partial h}{\partial y} = w \tag{6}$$

where $h(x, y, t)$ is the wave height with respect to the undisturbed free surface, and (u, v, w) are the Cartesian velocity on a free surface.

On the free surface, two co-ordinate systems may be chosen. One is for the body-fitted co-ordinate system, in which Equation (6) has to be transformed. Consequently, a finite difference (FD) approach is easy to implement. This is the hybrid Cartesian/curvilinear approach for the bulk RANS flow and the free surface, respectively. It has been successfully applied to our viscous free-surface calculations [2, 22, 32]. Therefore, an outline with additional features associated with the application of the Cartesian co-ordinate system is given using a cell-centred finite-volume (FV) method. This is desirable, since the discretization is compatible with the current procedure of solution of the RANS equations.

A cell-centred FV approach with the ENO scheme: Using the Gauss theorem, a 2D wave equation (6) can be written as

$$\frac{\partial}{\partial t}\int_V h\,\mathrm{d}V + \int_S (n_x u + n_y v)h\,\mathrm{d}S = \int_V w\,\mathrm{d}V \tag{7}$$

where V is the volume of a cell and S is the corresponding area of the cell face. n_x and n_y are the components outwards normal to the face in the x- and y-directions, respectively. With the mid-point rule approximation, the integration for each cell yields

$$\frac{\partial h}{\partial t} + \frac{1}{V}\{(Uh)_e - (Uh)_w + (Uh)_n - (Uh)_s\} = w \tag{8}$$

where the subscripts (e,s,w,n) denote the notation at the corresponding face (see Figure 2). For example, $U_e = (S^x u + S^y v)_e$ at the east (e) face. S^x and S^y are the components of the area vector. These are calculated with the spatial co-ordinates (x, y), respectively,

$$S^x = Sn_x = y_{ne} - y_{se} \quad \text{and} \quad S^y = Sn_y = -(x_{ne} - x_{se}) \tag{9}$$

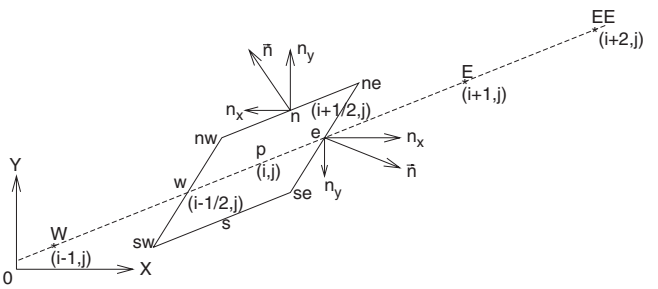

Figure 2. A usual notation in a control volume.

In general, the values of the solution variables on the face are obtained with a linear interpolation technique. In this case, u_e and v_e at the east face are estimated as averages of the neighbouring node values:

$$u_e = \frac{1}{2}(u_P + u_E) \quad \text{and} \quad v_e = \frac{1}{2}(v_P + v_E) \tag{10}$$

For the wave height at the face, a second-order essential non-oscillation (ENO) scheme [19] is chosen. This achieves a second-order accuracy for the convective fluxes by introducing more upwind points.

Using the ENO approach, for example, the left and right states $h^{\mathrm{L}}_{i+1/2,j}$ and $h^{\mathrm{R}}_{i+1/2,j}$ at the e face are given by

$$h^{\mathrm{L}}_{i+1/2,j} = h_{i,j} + \frac{1}{2}m(\triangle_{i+1/2,j}, \triangle_{i-1/2,j}), \quad h^{\mathrm{R}}_{i+1/2,j} = h_{i+1,j} - \frac{1}{2}m(\triangle_{i+2/3,j}, \triangle_{i+1/2,j}) \tag{11}$$

where $\triangle_{i+1/2,j} = h_{i+1,j} - h_{i,j}$ and the similar expressions in Equation (11) are easy to evaluate with index substitution. The function $m(a,b)$ is defined as

$$m(a,b) = \begin{cases} a & \text{if } |a| \leqslant |b| \\ b & \text{otherwise} \end{cases} \tag{12}$$

Dependent on the sign of U_e, we choose

$$h_{i+1/2,j} = \begin{cases} h^{\mathrm{R}}_{i+1/2,j} & \text{if } U_e \leqslant 0 \\ h^{\mathrm{L}}_{i+1/2,j} & \text{otherwise} \end{cases} \tag{13}$$

$h_{i-1/2,j}$ at the face $(i-\frac{1}{2}, j)$ is constructed in an identical fashion.

The second-order explicit Adams–Bashforth formulation is implemented for the time integration once the fluxes at four faces are obtained.

$$h^{n+1} = h^n + \Delta t\left(\frac{3}{2}f^n - \frac{1}{2}f^{n-1}\right) \tag{14}$$

where the superscripts $(n-1, n, n+1)$ indicate the previous, current and next time level, respectively, Δt is the local time step, and the source term (f) is written as $f = w - 1/V\sum_{i=1}^{4}(uS^x + vS^y)h$. During the free-surface calculation, surface particles on the free

surface are enforced when moving in the vertical direction. This requires a relatively small time step in order to ensure the accuracy of the computation.

2.3.2. The dynamic boundary conditions. The dynamic boundary conditions represent the continuity of the stress on a free surface. For a turbulent flow, the stress tensor σ_{ij} is written as

$$\sigma_{ij} = -p\delta_{ij} + \mu\left(\frac{\partial u_i}{\partial x_j} + \frac{\partial u_j}{\partial x_i}\right) - \rho\overline{u_i' u_j'} \tag{15}$$

where $\rho\overline{u_i' u_j'}$ is the Reynolds stress. With the eddy viscosity approximation, Equation (15) can be reduced to

$$\sigma_{ij} = -p\delta_{ij} + \frac{1}{R_{\text{eff}}}\left(\frac{\partial u_i}{\partial x_j} + \frac{\partial u_j}{\partial x_i}\right) \tag{16}$$

where R_{eff} is the effective Reynolds number ($1/R_{\text{eff}} = 1/R_n + \gamma_t$), γ_t is the dimensionless turbulent kinetic viscous coefficient, and p is the total pressure defined as $p = \psi - \frac{2}{3}k - z/F_n^2$, where ψ is the so-called piezometric pressure. $R_n = U_0 L/v$ and $F_n = U_0/\sqrt{gL}, g$ is the acceleration of gravity.

Since $n_i\sigma_{ij}n_j, n_i\sigma_{ij}t_j^1$ and $n_i\sigma_{ij}t_j^2$ are one local normal component and two tangential components of the surface forces at a free surface, respectively, the normal and tangential dynamic free-surface conditions may be derived through balancing these force components. t_i^1 and t_i^2 are the tangential vectors in the (x,z)- and (y,z)-planes, respectively. n_i is the ith components of the normal vector on a free surface, which can be expressed in terms of the wave height (h):

$$\mathbf{n} = (n_x, n_y, n_z) = \frac{(-h_x, -h_y, 1)}{(h_x^2 + h_y^2 + 1)^{1/2}} \tag{17}$$

The Reynolds stress free-surface boundary conditions (RSFSBC): (1) *Zero effective shear stress.* Surface tension could be dropped due to a very high R_n. The tangential stress at the free surface should be zero without a wind. Thus, two tangential dynamic free-surface conditions are written as

$$n_i\tau_{i1} = 0 \quad \text{and} \quad n_i\tau_{i2} = 0 \tag{18}$$

with

$$\tau_{ij} = \frac{1}{R_{\text{eff}}}\left(\frac{\partial u_i}{\partial x_j} + \frac{\partial u_j}{\partial x_i}\right) \tag{19}$$

Using the relationships of Equations (17) and (19), and setting $(x_1, x_2, x_3) = (x, y, z)$ and $(u_1, u_2, u_3) = (u, v, w)$, these can be reduced to

$$\frac{\partial u}{\partial z} = -\frac{\partial w}{\partial x} + 2\frac{\partial h}{\partial x}\frac{\partial u}{\partial x} + \frac{\partial h}{\partial y}\left(\frac{\partial u}{\partial y} + \frac{\partial v}{\partial x}\right) \tag{20}$$

$$\frac{\partial v}{\partial z} = -\frac{\partial w}{\partial y} + \frac{\partial h}{\partial x}\left(\frac{\partial u}{\partial y} + \frac{\partial v}{\partial x}\right) + 2\frac{\partial h}{\partial y}\frac{\partial v}{\partial y} \tag{21}$$

(2) *Normal dynamic free-surface condition*. Assuming negligible surface tension again, the condition that jumps in the normal direction leads to

$$n_i \sigma_{i3} = 0 \tag{22}$$

Substituting Equations (16) and (17) into Equation (22), it can be rewritten as

$$\psi = \frac{h}{F_n^2} + \frac{1}{R_{\text{eff}}} \left\{ 2 \frac{\partial w}{\partial z} - \frac{\partial h}{\partial x} \left(\frac{\partial u}{\partial z} + \frac{\partial w}{\partial x} \right) - \frac{\partial h}{\partial y} \left(\frac{\partial v}{\partial z} + \frac{\partial w}{\partial y} \right) \right\} \tag{23}$$

Generally, the value of $\frac{2}{3} k$ is too small. As a result, it has been ignored in our computations. With Equations (20)–(23), the pressure (ψ) and the components (u, v) of the velocities on the free surface are evaluated. The continuity equation is introduced for the determination of the component w of the velocity:

$$\frac{\partial w}{\partial z} = -\frac{\partial u}{\partial x} - \frac{\partial v}{\partial y} \tag{24}$$

We call Equations (20)–(24) as the Reynolds stress free-surface boundary conditions (RSFSBC) due to consideration of viscosity on the free-surface boundary conditions. These are the Neumann boundary conditions for the velocities on the free surface. The corresponding derivatives in these equations are approximated with a central difference scheme. At node $P(i, j)$ (see Figure 2), for example the term of the left-hand side in Equation (24) may be written as follows using a cell-centred finite-volume (FV) method.

$$\left(\frac{\partial w}{\partial z} \right)_{i,j,k} = \frac{1}{V} \sum_{i=1}^{6} (n_z S) w = \frac{1}{V} \sum_{i=1}^{6} S^z w \tag{25}$$

where S^z is the component of the area vector in the z-direction. The sum is taken over six faces of a hexahedral cell with the help of the ghost cell. In this way, the derivative of the velocities with respect to the z-direction is expressed as

$$\begin{aligned} V \left(\frac{\partial \varphi}{\partial z} \right)_{i,j,k} &= (S^z \varphi)_{\text{top}} - (S^z \varphi)_{\text{bottom}} + (S^z \varphi)_{\text{right}} - (S^z \varphi)_{\text{left}} \\ &\quad + (S^z \varphi)_{\text{front}} - (S^z \varphi)_{\text{back}} \end{aligned} \tag{26}$$

where the subscripts (top, bottom, right, left, front, back) indicate the notation for the corresponding faces and $\varphi = (u, v, w)$. The first two terms are located at the centre of the ghost cell adjacent to the free surface and interior cell of the flow, respectively. The others are over the face of a cell on the free surface, which will be used as part of the source terms. Note that all the values at the faces on the free surface are determined with a linear interpolation at the both sides of the corresponding node. But, for the velocity at the centre of the ghost grid, an one-side extrapolation along the free-surface cell and the first cell inside the flow is implemented.

The inviscid free-surface boundary conditions (IFSBC): If the free-surface boundary layer is neglected and gradients of the velocity are assumed to be zero, thus, this leads to the inviscid dynamic boundary conditions that have been widely applied in the literature [4, 5, 22]

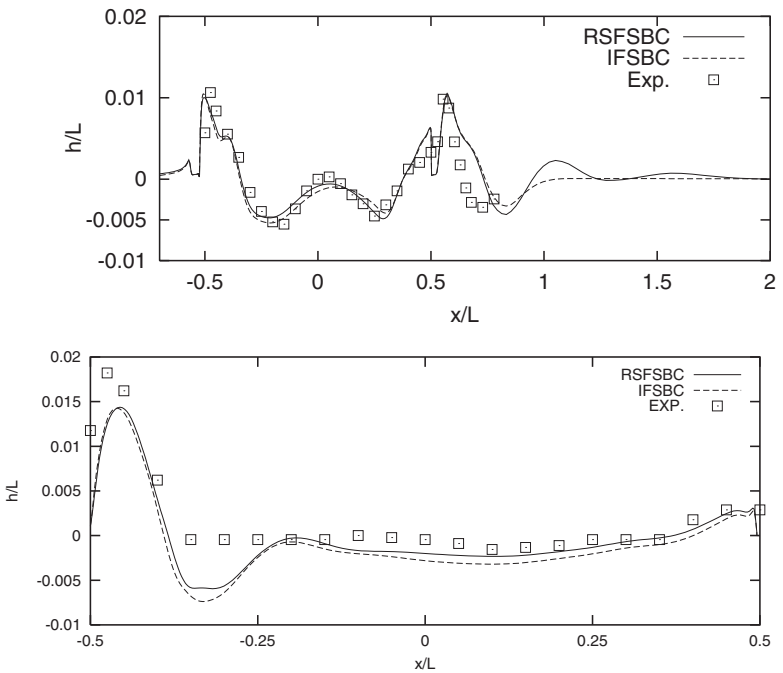

Figure 3. Comparison of the surface-wave profiles between the RSFSBC and the inviscid free-surface boundary conditions (IFSBC). Top: the KCS model ($F_n = 0.26$ and $R_n = 14 \times 10^6$; grid with $161 \times 161 \times 65$; using Baldwin–Lomax's model). Bottom: the DTMB 5415 model ($F_n = 0.28$ and $R_n = 12.8 \times 10^6$; grid with $191 \times 161 \times 33$; using the k–ε model).

due to its simplicity. In this way, three components of the Cartesian velocities are extrapolated with gradients of zero-normal velocity from the interior of the flow by

$$\frac{\partial u}{\partial n} = \frac{\partial v}{\partial n} = \frac{\partial w}{\partial n} = 0 \tag{27}$$

and the pressure ψ is determined from

$$\psi = \frac{h}{F_n^2} \tag{28}$$

Equations (27) and (28) are named as the IFSBCs. Generally, both the viscous and inviscid conditions can be applied for determination of the velocities and the pressure on the free surface. Two examples are given for the wave profiles along the hull surface with these two boundary conditions: the KCS model and the DTMB 5415 model (see Figure 3). By comparison with the IFSBC, the RSFSBC (the Reynolds-stress free-surface boundary conditions) can give the accurate prediction. Although the computations with the RSFSBC are somewhat complex due to the strong coupling of the free surface with a turbulent flow, its use helps to capture well wake dynamics, and appreciable errors introduced through approximating the RSFSBC may be avoided [33]. Furthermore, the prominent feature of the free surface like the vortex can be generated [34–36].

2.4. Solution of the bulk flow and the free surface

With a collocated grid arrangement, all the solution variables are located at the centre of a cell. An uncoupled approach is employed, where all the boundary conditions are given explicitly. In the course of the iterative procedure, the Roe's approach [37] with the *MUSCL* type and a central-difference scheme are separately implemented for the evolution of the inviscid and viscous fluxes. The solution vectors are updated by the *DDADI*-factorization with the local time step. The convergence rate is improved by the V-cycle of the multigrid method. Once the solutions for the bulk RANS flow are given [27], the spatial derivative on the free surface is evaluated with the *ENO* scheme. The wave elevation is renewed with the second-order explicit Adams-Bashforth scheme. A new volumetric grid is generated based on the updated wave height [38]. This procedure is repeated at each iterative cycle until the steady state is attained. The numerical scheme in detail is provided in [22].

2.5. A model of treatment of the near-wall free surface

As mentioned before, the integration of the KFSBC at the so-called contact line will involve the singular solution. For a turbulent flow, extrapolation of the wave elevation at the first cell to a hull surface does not work well due to oscillations of the waves induced by a high aspect ratio within the boundary layer. In our model, we choose the near-wall narrow strip rather than the width of a single cell. It is kept as a constant for entire time, which is similar to the approach proposed by Wilson *et al.* [5] and Sussman and Osher [19]. The free surface on this strip is assumed to be continuous and smooth. Therefore, one possibility is to extrapolate linearly the near-wall free surface without the solution of Equation (6). A linear least-square fit scheme may be used for this purpose. The problems related to oscillations of the wave systems and the numerical singularity could be avoided. Furthermore, the local filtering that covers this strip is required in order to prevent spurious noise of the waves and keep the width of the strip as small as possible (an order of magnitude is about $y/L \approx 10^{-4}$ for all test cases). Our computations demonstrate that this approach can maintain stabilization of the free surface and achieve good surface wave profiles. This is because in our previous work [26], we have to use a rather large strip for interpolation of the wave elevation near the hull surface due to strong oscillations of the waves in this area; therefore, a bow wave along the hull surface is not captured well.

A transom itself causes the singularity of a flow. Additionally, a flow off the transom is always complex due to an unsteady turbulence in the wake. These may induce oscillations of the free surface. To prevent numerical instability, the dry-transom model [22] was applied for treatment of the free surface in the finite region close to a transom. It can work perfectly once a transom is dry at the beginning of the computation. Therefore, we will use this model in the contain ship (the KCS model) case. In this way, the wave height at the transom profile is set equal to its depth without an interpolation procedure due to the enforcement of the detachment of a flow at the transom corner. Unfortunately, it will fail to work once a transom is immersed in a flow at rest. In our present work, we have developed a new model and hope that it can work effectively in case one does not know *a priori* whether a transom is dry or wetted. It will be tested in the cases of the combatant (the DTMB 5415 model) and tanker with a partially wetted transom. In this model, the surface-wave height is evaluated with extrapolation, and the transom at the final state may expose completely or immerse partially. We call this one as a general-transom model due to no limit for a flow and an initial state

Table II. Computational conditions and grid for three test cases.

	The KCS model	The DTMB 5415 model	The tanker model
F_n	0.26	0.28	0.15
R_n	14×10^6	12.8×10^6	8.727×10^6
Coarsest mesh	$41 \times 41 \times 17$	$49 \times 41 \times 9$	$35 \times 29 \times 13$
Fine mesh	$81 \times 81 \times 33$	$97 \times 81 \times 17$	$69 \times 57 \times 25$
Finest mesh	$161 \times 161 \times 65$	$193 \times 161 \times 33$	$137 \times 113 \times 49$

of geometry. As expected, it may replace the dry-transom model in the near future, although our dry-transom model did well in some cases. More details of the model for the near-wall free-surface treatment can be seen in Reference [39].

3. COMPUTATIONAL CONDITIONS AND GRIDS FOR THREE TEST CASES

Two benchmark test cases [40] are two classes of typical modern surface ships. One is the KCS model of the KRISO container ship (Korea). Another is the DTMB 5415 model of a US Navy combatant (USA). They are slender hull forms equipped with a bulbous bow/a sonar dome and a transom stern. Additionally, a modern full hull form tanker model from the Kvaerner Masa-Yards, Finland, is also included in this study. The computational conditions (see Table II) correspond with the measurements from Instituto Nazionale per Studi ed Esperienze di Architettura Navale (INSEAN), Italy, Korea Research Institute for Ships and Ocean Engineering (KRISO), Korea, and the shipyard, the Kvaerner Masa-Yards, Finland. The DTMB 5415 model is free to trim and sink but the tanker model and the KCS models are fixed. Since the effect of a free surface is thought to be relatively small at a low speed for the tanker model, we still use the IFSBC for determination of the pressure and the velocity on the free surface instead of the RSFSBC, which will be used in the KCS model and the DTMB 5415 model cases.

Three grid levels with a grid refinement ratio (r) of 2 (that is, $r=2$) are applied for the computations. This is a doubled mesh in each direction. The total number at the finest mesh is about 1 million. The distribution of the grid points in the x-, y- and z-directions is given by Table II, such as $(I \times J \times K) = (161 \times 161 \times 65)$ for the KCS model. The steady-state solution on the coarse grid is used as an initial guess for the fine solution, which leads to the low CPU time (each case approximates 4 or 5 days at the finest mesh). The computational domain is about $-3 \leqslant x/L \leqslant 6$, $0 \leqslant y/L \leqslant 3$ and $-3 \leqslant z/L \leqslant h_{\max}$ (the calculated maximum wave height). A single O–O topology grid is employed (see Figure 4). With this grid topology, both the general- and dry-transom models can be used, where the dry-transom model was used for the KCS model, and the general-transom model was used for the DTMB 5415 model and the tanker model.

One-half of the hull is considered for the computations since the hulls are symmetric. All calculations were carried out on a Silicon Graphics Origin2000 provided by the Center for Scientific Computing (CSC), Finland. In the entire text, all variables are made dimensionless with the ship length L, the free-stream velocity U_0 and the density ρ.

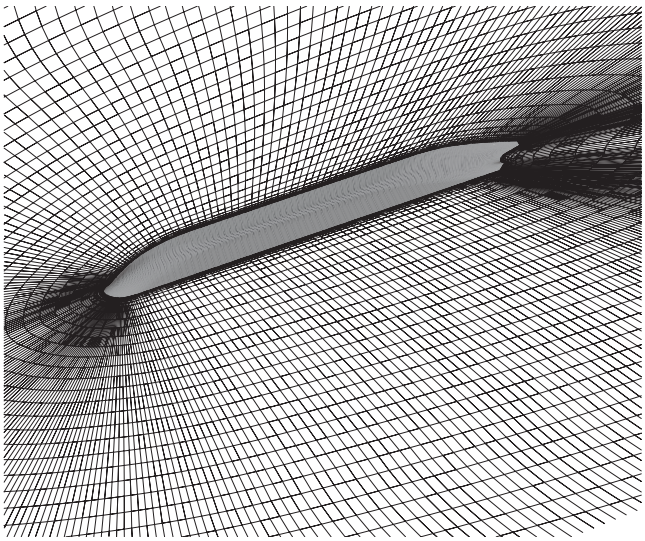

Figure 4. A single O–O structured mesh.

4. CALCULATED RESULTS FOR THREE TEST CASES

Validation procedures will be demonstrated with three test cases: the KCS model, the DTMB 5415 model and the tanker model, using the k–ε model and Baldwin–Lomax's model [41], after the convergence performances and the grid refinement studies are investigated.

4.1. Convergence history

Iterative convergence in this case is assessed by examining the L_2 norm of the residuals (Res) for the momentum (U, V, W) in the x-, y- and z-directions, and the pressure (P) at the finest mesh, respectively,

$$\mathrm{Res}_{\varphi} = \left[\sum_{i=1}^{N} (\varphi_{i,j,k}^{n} - \varphi_{i,j,k}^{n-1})^2 / N^2 \right]^{1/2}$$

where the superscripts $(n, n-1)$ denote the different time level, N is the total number of a cell and φ represents (U, V, W, P).

We draw the curves of the L_2 norm of the residuals against iterative cycles (see Figure 5). The residuals for (U, V, W) display a faster convergence rate than that for P, as shown in Figure 5. Furthermore, all residuals at any grid point come down and they lie between 10^{-4} and 10^{-5} for P or below 10^{-5} for (U, V, W) at the final state, respectively. This implies that it may be sufficient to achieve an approximately divergence-free solution for a given level of convergence. Two turbulence models, Chien's k–ε model and Baldwin–Lomax's model, are used for the computations. For the DTMB 5415 model and the tanker model, the k–ε model is used. Baldwin–Lomax's turbulence model is used for the KCS model. This model has been successfully applied to our previous work [22], including investigation of the convergence performances on three consecutive grids with $r = 2$ [21].

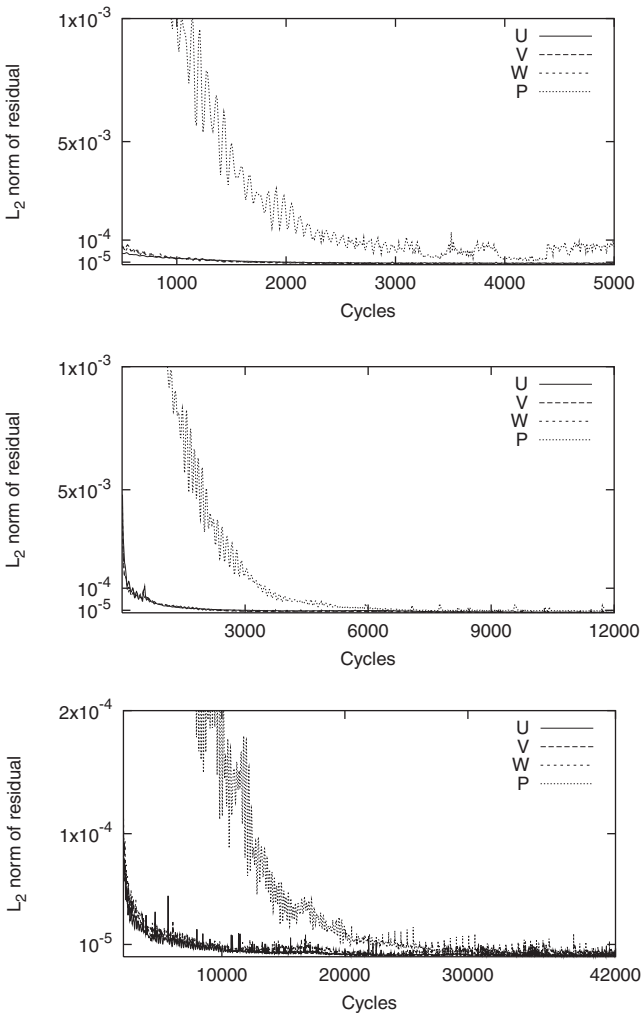

Figure 5. Convergence histories of the L_2 norm of the residuals (U, V, W, P) at the finest mesh. Top: the KCS model ($F_n = 0.26$ and $R_n = 14 \times 10^6$; grid with $161 \times 161 \times 65$; using Baidwin–Lomax's model). Middle: the DTMB 5415 model ($F_n = 0.28$ and $R_n = 12.8 \times 10^6$; grid with $193 \times 161 \times 33$; using the k–ε model). Bottom: the tanker model ($F_n = 0.15$ and $R_n = 8.727 \times 10^6$; grid with $137 \times 113 \times 49$; using the k–ε model).

4.2. Grid refinement study

The grid refinement studies are investigated on three different grids ($r = 2$, see Table II). The averaged y^+ values at the first grid from the coarsest to the finest are 2.4, 1.2 and 0.6 for the KCS model, 6.0, 3.0 and 1.5 for the DTMB 5415 model, and 0.8, 0.4 and 0.2 for the tanker model, respectively. The results are presented in terms of the wave profiles and the wave contours. According to a usual tradition, we define $x/L = -0.5$ and 0.5 as the location of the bow and the transom stern in all the corresponding figures, respectively.

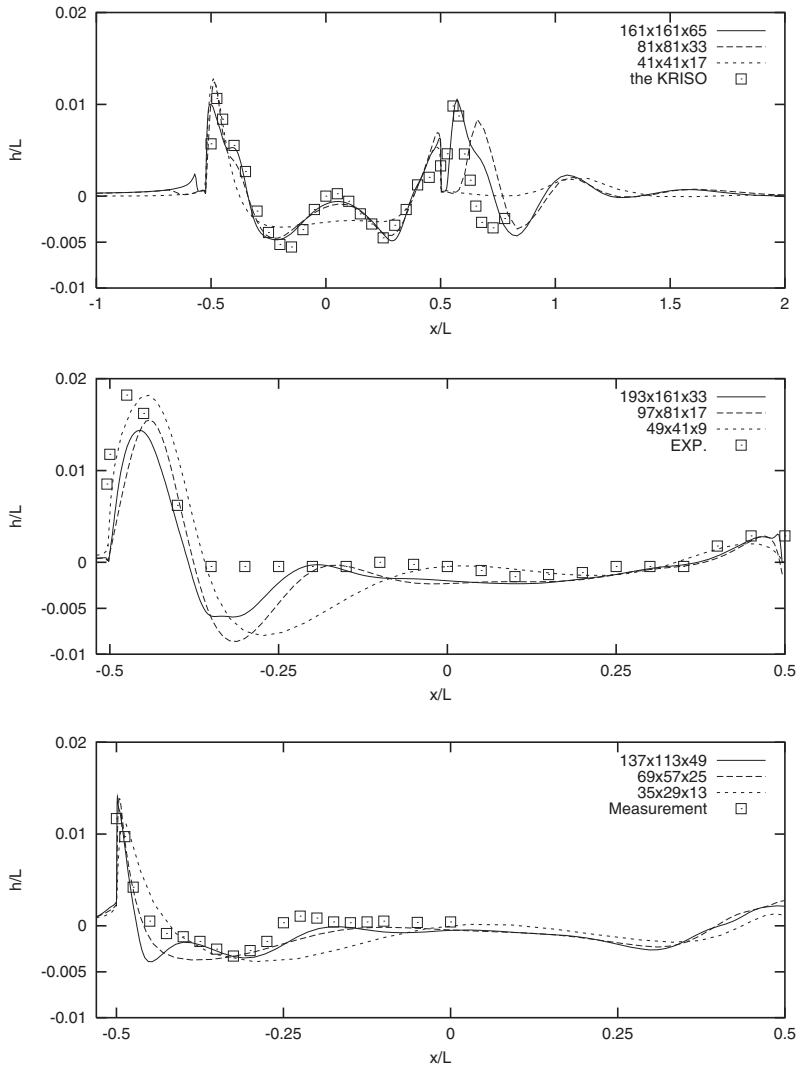

Figure 6. Surface-wave profiles at three grid levels. Top: the KCS model ($F_n = 0.26$ and $R_n = 14 \times 10^6$; using Baldwin–Lomax's model). Middle: the DTMB 5415 model ($F_n = 0.28$ and $R_n = 12.8 \times 10^6$; using the k–ε model). Bottom: the tanker model ($F_n = 0.15$ and $R_n = 8.727 \times 10^6$; using the k–ε model).

4.2.1. Wave profiles. Figure 6 illustrates the surface-wave profiles compared on three different grids for these three test cases, respectively. The difference between the middle and the fine meshes is relatively small. On the coarsest grid, the wave systems cannot be detected well, as shown in Figure 6. It is observed that the essential very generous details may be captured with the fine mesh. Moreover, as the grid is refined systematically, the results can be closer to the experimental data. Obviously, the maximum discrepancy between two fine meshes occurs at the first peak off the transom stern for the KCS model and the first trough for the DTMB 5415 model and the tanker model.

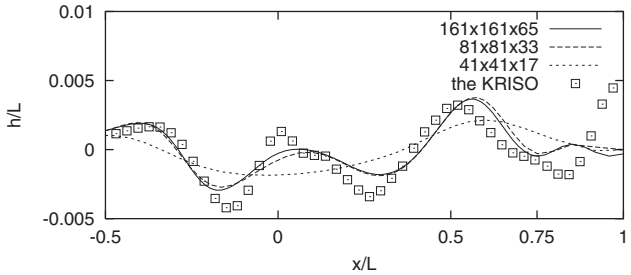

Figure 7. Longitudinal wavecuts ($y/L = 0.1509$) at three grid levels, the KCS model ($F_n = 0.26$ and $R_n = 14 \times 10^6$). Using Baldwin–Lomax's model.

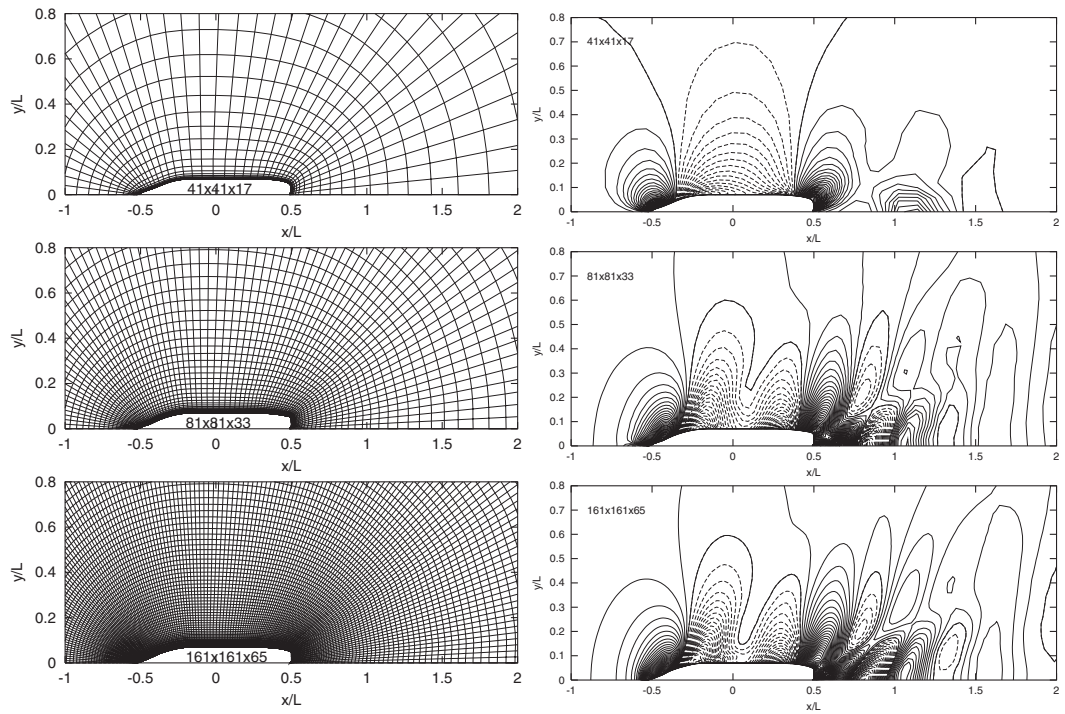

Figure 8. Free-surface mesh and the wave contours at three grid levels, the KCS model ($F_n = 0.26$ and $R_n = 14 \times 10^6$). Solid lines for crests; dashed lines for trough; levels: 0.0002. Using Baldwin–Lomax's model.

According to the longitudinal wavecuts, we further analyse the grid refinement effects. Figure 7, for example, exhibits the results at $y/L = 0.1509$ for the KCS model. The gap between two fine meshes is still small. By comparison with the measurements, both amplitude and phase between $x/L = -0.2$ and 0.3 are not very well predicted, especially in the wake ($0.75 < x/L \leqslant 1.0$), where the waves are rapidly damping (see Figure 7). On the other hand, the current finest grid does not seem to help. Some reasons may be interpreted as unsteady

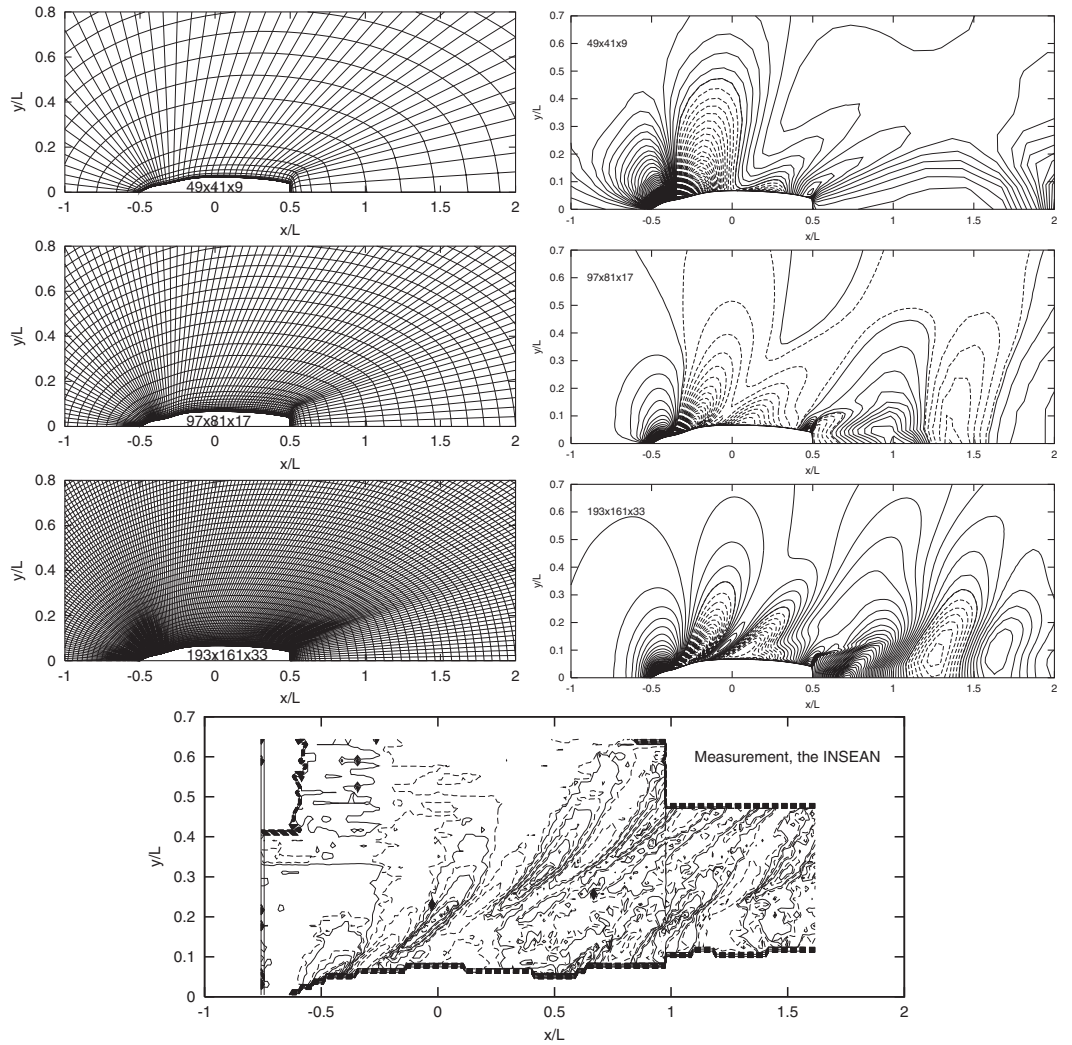

Figure 9. Free-surface mesh and wave contours at three grid levels, the DTMB 5415 model ($F_n = 0.28$ and $R_n = 12.8 \times 10^6$). Solid lines for crests; dashed lines for trough; levels: 0.0002. Using the k–ε model.

complicated wake flows. Thus, more grid points are required for accurate prediction of the solution in this area.

Overall, the results at the finest mesh can be compared with the experimental data. The influences of the grid density on the wave profiles are sensitive with the current three grid levels for all test cases. But, the two fine meshes can describe the wave elevation, especially at the finest mesh. This suggests at least two refined grid levels are required in order to test asymptotic grid convergence. Probably, a fine mesh should contain at minimum approximate 10^5 nodes on the basis of our computations, and most are distributed along the x- and y-directions dependent on physical phenomena on the free surface. Furthermore, the bow wave

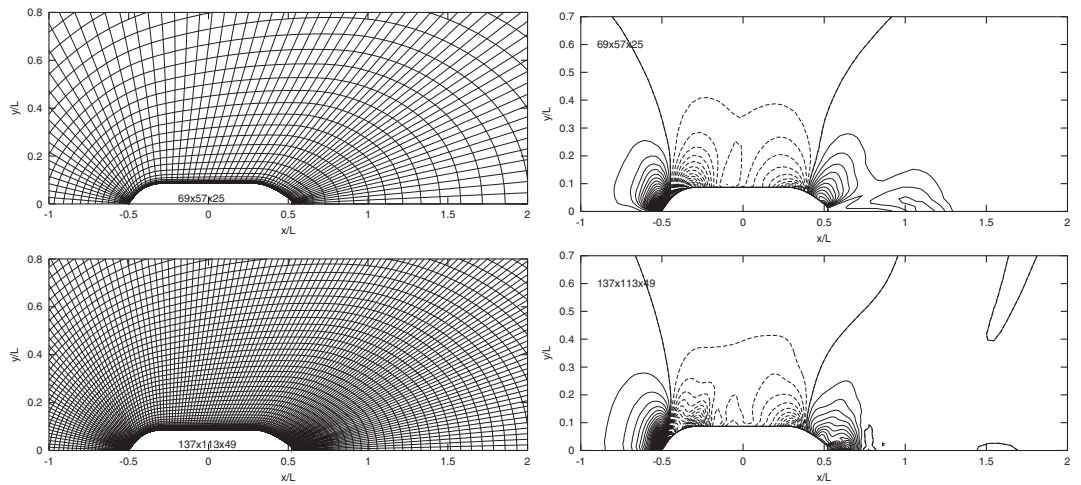

Figure 10. Free-surface mesh and wave contours at two fine levels, the tanker model ($F_n = 0.15$ and $R_n = 8.727 \times 10^6$). Solid lines for crests; dashed lines for trough; levels: 0.0002. Using the k–ε model.

is reproduced for the KCS model and the tanker model, while this peak is underestimated and the first trough becomes too deep for the DTMB 5415 model.

4.2.2. Wave contours. The wave contours at the corresponding grid levels are shown in Figures 8–10 for three test cases. There is a relatively large difference at the present grid size, especially in the region close to the transom (see Figures 9 and 10). In general, a lot of nodes have to be located in this area to capture the waves. As expected, the amplitudes of the waves at the crest, the shoulder and the trough show closer agreement with the experimental data as the grid is refined systematically, such as see Figure 13 for the measurements from the KRISO. Furthermore, the detailed features of the wave systems are illustrated well at the finest mesh. Nevertheless, in the remote wake, the damping of the far-field waves is obvious due to the effects of the grid size, where the grid density on the free surface is insufficient (see Figures 8–10). Further investigation is required to clarify the issue.

We also give a perspective view of the free-surface waves (see Figure 11). This provides a straightforward observation for the wave elevation in the region of interest.

4.3. Effects of turbulence models on waves

We studied the influence of two turbulence models, the k–ε model and Baldwin–Lomax's model, on the wave systems. An example is given for the KCS model. Other two cases can be seen in our final report [39]. It is found that the overall tendency of the wave systems is very similar for these two turbulence models. There is a certain effect on the waves, as shown in Figures 12 and 13.

First, for the surface-wave profiles (see the top of Figure 12), the shoulder wave is predicted well, especially with Baldwin–Lomax's model, where it lies behind the bow peak ($x/L = -0.5$).

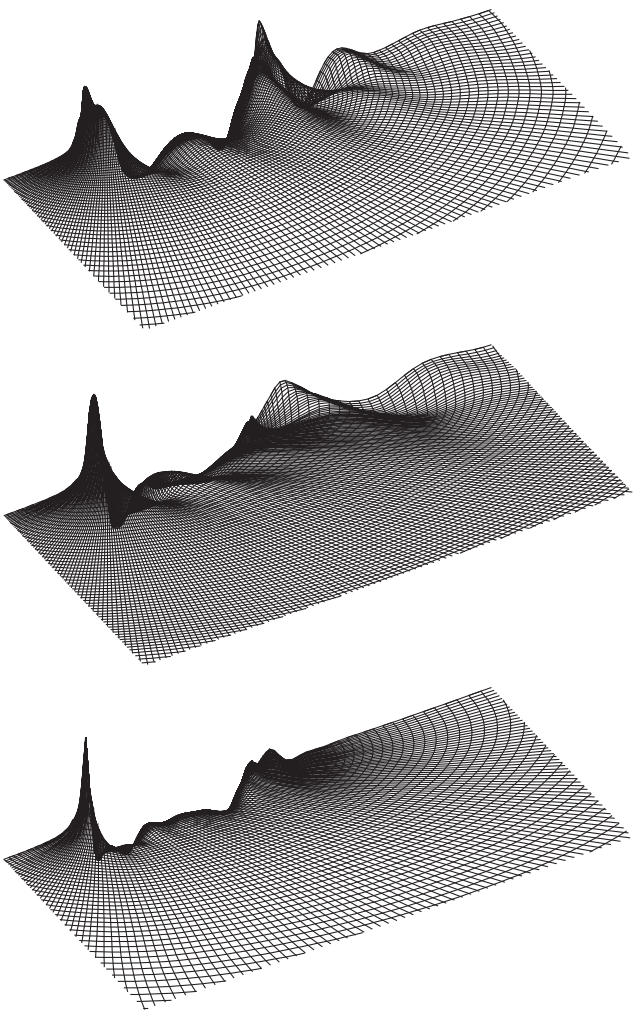

Figure 11. Perspective view of the wave stationary at the finest mesh. Top: the KCS model ($F_n = 0.26$ and $R_n = 14 \times 10^6$). Middle: the DTMB 5415 model ($F_n = 0.28$ and $R_n = 12.8 \times 10^6$). Bottom: the tanker model ($F_n = 0.15$ and $R_n = 8.727 \times 10^6$).

Secondly, the first and second crests can be observed. The magnitude and the phases are almost the same as observed in the measurements. Unfortunately, there is a large departure from the stern wave ($x/L = 0.5$). Since the flow adheres to the transom surface at the steady-state as observed during the experiment, the assumption of enforcing a flow to detach at the transom corner may overestimate this one. Interestingly, the peak behind the transom ($0.5 \leqslant x/L \leqslant 1.2$) can be reproduced, especially for Baldwin–Lomax's model, as shown in Figure 12, while the results with k–ε look more promising as compared to those with Baldwin–Lomax model. Overall, our results confirm that the implementation of the dry-transom model does not seem to yield results with more loss of accuracy than the general-transom model. As a result, it may be used as one of the tools for the treatment of the transom flows.

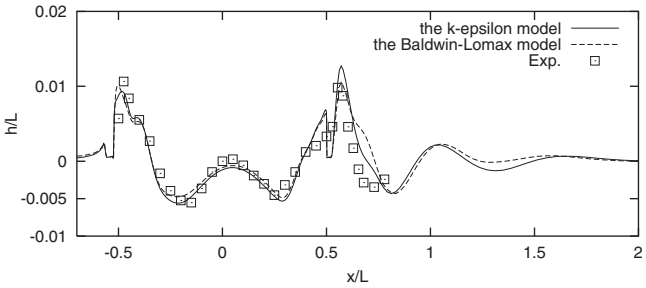

Figure 12. Effects of the k–ε model and Baldwin–Lomax's model on the surface wave profiles, the KCS model ($F_n = 0.26$ and $R_n = 14 \times 10^6$).

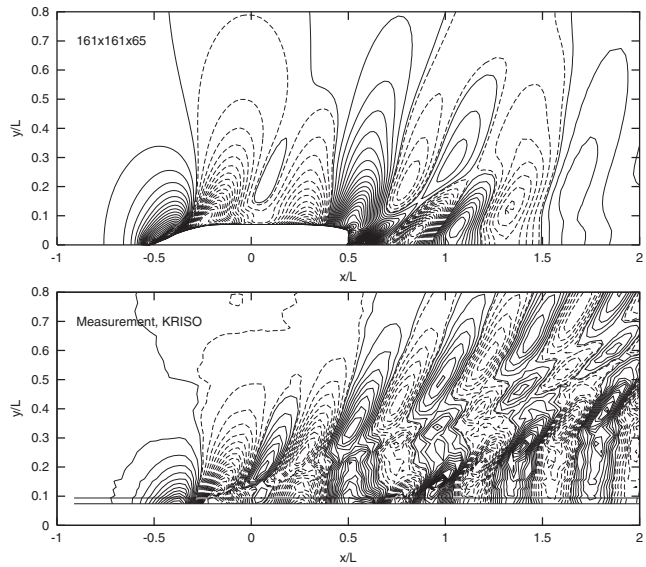

Figure 13. Wave contours with the k–ε model, the KCS model ($F_n = 0.26$ and $R_n = 14 \times 10^6$). Solid lines for crests; dashed lines for trough; levels: 0.0002.

Additionally, the computations with the k–ε model improves the wave contours as compared to the results with Baldwin–Lomax's model, as shown in Figures 8 and 13. Nevertheless, the discrepancy between them is relatively small.

4.4. Wake at the propeller disk

Figure 14 displays the velocity vectors (v, w) and the axial-velocity (u) contours in the propeller plane ($x/L = 0.4825$) for the KCS model and ($x/L = 0.435$) for the DTMB 5415 model, respectively. The measurements are from the KRISO experimental fluid dynamic (EFD) data and the INSEAN. By comparison with the measurements, the results look fine for both cases. As expected, the thick boundary layer is captured at this plane, such as $u/U_0 = 0.9$ for the

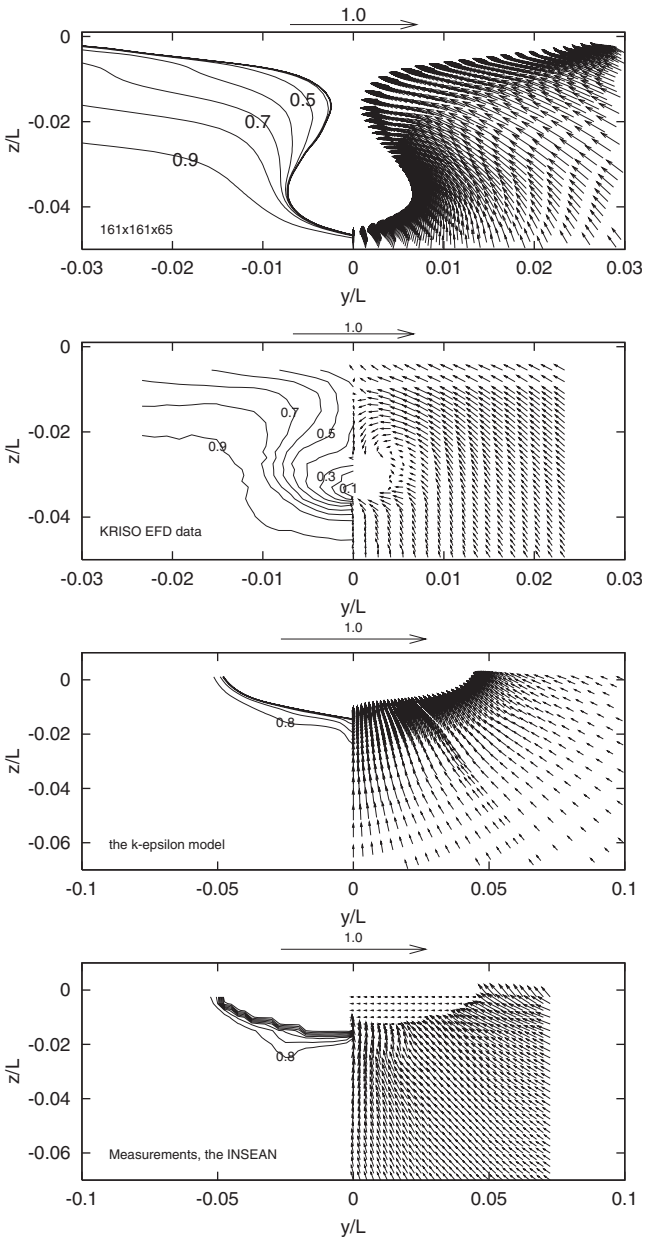

Figure 14. Comparison of calculated axial-velocity (u) contours and the velocity vectors (v, w) at the propeller disk with the measurements. Top: the KCS model ($F_n = 0.26$ and $R_n = 14 \times 10^6$; using Baldwin–Lomax's model). Bottom: the DTMB 5415 model ($F_n = 0.28$ and $R_n = 12.8 \times 10^6$; using the k–ε model).

KCS model and 0.8 for the DTMB 5415 model. In general, the gross features of the flow disturbance observed during the experiment can be reproduced. Note that a vortex at the core of the propeller disk is not created for the KCS model. The reason may be due to the fact that the dummy hub was not considered in the computations, but it is attached during the experiment for this case.

5. CONCLUSIONS

We have presented our calculated results for three types of typical modern ships in modelling the ship-generated waves using the FINFLO-RANS solver. Validation studies have been demonstrated with three modern vessels: a container ship (the KCS model), a US navy combatant (the DTMB 5415 model) and a tanker. The results are compared with the measurements in terms of the wave profiles, wave pattern and turbulent flow with two turbulence models, Chien's low Reynolds number k–ε model and Baldwin–Lomax's model. Additionally, it is found that two turbulence models employed can give almost the same tendency for the wave patterns and the difference between them is small. With three different grids ($r = 2$), the convergence performances and the grid refinement study have been investigated. Two fine meshes give the nice results. As the grid is refined systematically, the results agree with the experimental data.

Also, this paper outlines a procedure of numerical solution of the free surface using a cell-centred FV method with the ENO type, including the model for approximation of the free surface in the region close to the wall. One advantage is that it can maintain stabilization of the free surface and achieve a good result. Furthermore, a comparison between the viscous and inviscid dynamic free-surface boundary conditions has been made. Some improvement on the waves can be achieved with the viscous boundary conditions on the free surface. Overall, the method can yield detailed flow information on ship design.

In the near future, we will simulate the breaking waves based on a good idea proposed by Alessandrini [14], in which an artificial diffusion (adding a damping pressure to the normal dynamic free-surface condition, for example) is introduced so that the breaking waves are circumvented through absorbing energy of the waves. Of course, it is possible to implement the level set approach or the VOF method or both for this purpose. A parallel multiblock approach is being developed in order to reduce the CPU time. Furthermore, a local grid refinement approach could be applied for improvement of the solution of the far-field waves in the wake.

ACKNOWLEDGEMENTS

The present work is sponsored by the Technology Development Center (Tekes) in Finland and Finnish Shipbuilding Industry. The author would like to thank his supervisor, Prof. Jerzy Matusiak, who invites him to work in this project and provides very good working conditions. Thanks are given to the members of the CFD group at Helsinki University of Technology for their valuable help.

REFERENCES

1. Cowles G, Martinelli L. A viscous multiblock flow solver for free-surface calculations on complex geometries. *Proceedings of the 22nd Symposium on Naval Hydrodynamics*, Washington, DC, USA, 9–14 August 1998.

2. Li T, Matusiak J. Simulation of modern surface ships with a wetted transom in a viscous flow. In *Proceedings of the 11th International Offshore and Polar Engineering Conference*, vol. 4, Stavanger, Norway, 16–21 June 2001; 570–576.
3. Mascio ADi, Muscari R, Broglia R. Computation of the flow past the U.S. Navy combatant DTMB 5415 by a Godunov-type scheme. In *A Workshop on Numerical Ship Hydrodynamics*, Larsson L, Stern F, Bertram V (eds), Gothenburg, Sweden, 14–16 September 2000.
4. Beddhu M, Jiang M-Y, Whitfield DL, Taylor LK, Arabshahi A. CFD validation of the free surface flow around DTMB model 5415 using Reynolds averaged Navier–Stokes equations. *Third Osaka Colloquium on Advanced CFD Applications to Ship Flow and Hull Form Design*, Osaka, Japan, 25–27 May 1998; 215–227.
5. Wilson R, Paterson E, Stern F. Unsteady RANS CFD method for Naval combatant in waves. *Proceedings of the 22nd Symposium on Naval Hydrodynamics*, Washington, DC, USA, 9–14 August 1998.
6. Hino T. An interface capturing method for free surface flow computations on unstructured grids. *Journal of The Society of Naval Architects of Japan* 1999; **186**:177–183.
7. Hochbaum AC, Vogt M. Flow resistance prediction for a container ship. In *A Workshop on Numerical Ship Hydrodynamics*, Larsson L, Stern F, Bertram V (eds), Gothenburg, Sweden, 14–16 September 2000.
8. Sussman M, Dommermuth D. The numerical simulation of ship waves using Cartesian grid methods. *Proceedings of the 23rd Symposium on Naval Hydrodynamics*, in French, 18–21 September 2000.
9. Gueyffier D, Li J, Nadim A, Scardovelli R, Zaleski S. Volume-of-Fluid interface tracking with smoothed surface stress methods for three-dimensional flows. *Journal of Computational Physics* 1999; **152**:423–456.
10. Lin C, Percival S. Free surface viscous flow computation around a transom stern ship by Chimera overlapping scheme. *Proceedings of the 23rd Symposium on Naval Hydrodynamics*, vol. 3, in French, 18–20 September 2000; 14–27.
11. Tahara Y, Stern F. A large-domain approach for calculating ship boundary layers and wakes and wave fields for nonzero Froude number. *Journal of Computational Physics* 1996; **127**:398–411.
12. Gentaz L, Maury C, Alessandrini B, Delhommeau G. Numerical simulation of a two-dimensional wave tank in viscous fluid. *International Journal of Offshore and Polar Engineering* 2000; **10**:1–9.
13. Namin MN, Lin B, Faloner RA. An implicit numerical algorithm for solving non-hydrostatic free-surface flow problems. *International Journal for Numerical Methods in Fluids* 2001; **35**:341–456.
14. Alessandrini B, Gentaz L. A fully coupled theory for viscous free surface flow computation. In *A Workshop on Numerical Ship Hydrodynamics*, Larsson L, Stern F, Bertram V (eds), Gothenburg, Sweden, 14–16 September 2000.
15. Hodges BR, Street RL. On simulation of turbulent nonlinear free-surface flows. *Journal of Computational Physics* 1999; **151**:425–457.
16. Hino T. A study of grid dependence in Navier–Stokes solution for free surface flows around a ship hull. *Journal of The Society of Naval Architects of Japan* 1995; **176**:11–18.
17. ITTC. Report of the resistance and flow committee. In *22nd International Towing Tank Conference*, Seung-H Yang (ed.), Seoul, Korea and Shanghai, China, 5-11 September 1999; **1**:173–205.
18. Liu H, Ikehata M. Computation of free surface waves around an arbitrary body by a Navier–Stokes solver using the psuedocompressibility technique. *International Journal for Numerical Methods in Fluids* 1994; **19**: 395–413.
19. Sussman MS, Osher S. A level set approach for computing solutions to incompressible two-phase flow. *Journal of Computational Physics* 1994; **114**:81–124.
20. Haussling HJ, Miller RW, Coleman R. Computation of high speed turbulent flow about a ship model with a transom stern. *ASME FED SM*97, 1997.
21. Li T, Matusiak J. A refinement study of grid for turbulent ship free-surface flows. In *4th Numerical Towing Tank Symposium*, Bertram V (ed.), Hamburg, Germany, 23–25 September 2001.
22. Li T, Matusiak J, Lehtimäki R. Numerical simulation of viscous flows with free surface around realistic hull forms with transom. *International Journal for Numerical Methods in Fluids* 2001; **37**:601–624.
23. Ratcliffe T. Validation of free-surface Reynolds averaged Navier–Stokes and potential flow codes. *Proceedings of the 22nd Symposium on Naval Hydrodynamics*, Washington DC, USA, 9–14 August 1998.
24. Takafumi K, Miyata H. Simulation of non-linear ship flows by density-function method. *Journal of The Society of Naval Architects of Japan* 1994; **176**:1–10.
25. Bear TA, Cairncross RA, Schunk PR, Rao RR, Sackinger PA. A finite element method for free surface flows of incompressible fluids in three dimension, Part II. Dynamic wetting lines. *International Journal for Numerical Methods in Fluids* 2000; **33**:405–427.
26. Li T, Sänchez-Caja A, Martio J, Matusiak J. Simulation of free-surface viscous flow around two ship hulls using RANS solver FINFLO. In *A Workshop on Numerical Ship Hydrodynamics*, Larsson L, Stern F, Bertram V (eds), Gothenburg, Sweden, 14–16 September 2000.
27. Siikonen T. *FINFLO user guide*, *version 2.2*. Laboratory of Applied Thermodynamics, Helsinki University of Technology, Finland, 1998.
28. Chien K. Predictions of channel and boundary-layer flows with a low-Reynolds-number turbulence model. *AIAA Journal* 1982; **20**:33–38.

29. Menter FR. Zonal two-equation k–ω turbulence models for aerodynamic flow. *24th AIAA Computational Fluid Dynamics Conference*, (*Orlando Florida*), *AIAA Paper* 1993; 93-2906-CP.
30. Siikonen T. An application of Ros's flux-difference splitting for k–ε turbulence model. *International Journal for Numerical Methods in Fluids* 1995; **21**:1017–1039.
31. Patel VC. Ship stern and wake flows: status of experiment and theory. *Proceedings of the 17th ONR Symposium on Naval Hydrodynamics*, The Hague, The Netherland, 1988.
32. Li T, Matusiak J. Simulation of viscous flow of modern surface ships using the FINFLO RANS solver. In *The 8th International Symposium on Practical Design of Ships and Other Floating Structures*, You-Sheng Wu, Wei-Cheng Cui, Guo-Jun Zhou (eds), Shanghai, China, 16–22 September 2001; 413–420.
33. Choi JE, Stern F. Solid–fluid juncture boundary layer and wake with waves. *Proceedings of the 6th International Conference on Numerical Ship Hydrodynamics*, Iowa City, Iowa, 1993; 215–237.
34. Jeong Uh-Cheul, Doi Yasuski. Numerical study of vortical flows beneath the free surface around struts. *Journal of The Society of Naval Architects of Japan* 1996; **178**:23–31.
35. Lunder T, Koumoutsakos, Peteros. On the generation of vorticity at a free surface. *Journal of Fluid Mechanics* 1999; **382**:351–366.
36. Lian S, Zhang X, Yue Dick KP, Triantafyllou GS. The surface layer of free-surface turbulent flows. *Journal of Fluid Mechanics* 1999; **386**:167–212.
37. Roe PL. Approximate Riemann solvers, parameter vectors, and difference schemes. *Journal of Computational Physics* 1981; **43**:337–372.
38. Lehtimäki R. Grid deformation tools for simulation of free surface flows. In *6th International Conference on Numerical Field Simulation*, London, UK, 6–9 July 1998; 599–608.
39. Li T. Ship wavemaking in the context of a RANS-solver FINFLO-ship. *Report* M-270, Ship Laboratory, Helsinki University of Technology, Finland, 2002.
40. Gothenburg 2000. In *Workshop on Numerical Ship Hydrodynamics*, Larsson L, Stern F, Bertram V (eds), Gothenburg, Sweden, 14–16 September 2000.
41. Baldwin B, Lomax H. Thin layer approximation and algebraic model for separated turbulent flows. *AIAA paper* 1978; 78–257.

